JOURNAL OF COMPUTATIONAL PHYSICS 55, 129–153 (1984)

A Multicode Describing the Time Evolution of the Atomic Protium, Deuterium, and Tritium Densities in the First Wall of a Tokamak Reactor

A. NICOLAI AND D. REITER

Institut für Plasmaphysik der Kernforschungsanlage Jülich GmbH, Association EURATOM-KFA, P.O.B. 1913, D-5170 Jülich, West Germany

Received May 10, 1983; revised October 25, 1983

A multicode consisting essentially of three modules, the "first wall module," the "neutral gas module" and the "plasma module," is applied to compute the time evolution of the protium, deuterium and tritium densities within the wall of a fusion reactor. The first wall module describes the protium, deuterium and tritium diffusion implantation and trapping within and the recombination processes at the wall. The neutral gas module resorting to Monte-Carlo techniques computes the atomic and molecular flux densities hitting the wall. The plasma module calculates the parameters of the plasma background on the basis of the familiar transport equations. In the first wall module the predictor–corrector method is employed for solving the coupled system of diffusion equations with nonlinear boundary conditions. Nonanalogue methods, a combination of the tracklength and the collision estimator are applied in the neutral gas module to reduce the variance. As a specific example the code is applied to the first wall of an INTOR-like device.

1. INTRODUCTION

The permeation of protium or deuterium through a stainless-steel membrane at elevated temperatures had been treated both experimentally and numerically [1–8] and extrapolations to Tokamak reactors (INTOR) are available [9]. As far as the neutral gas background is concerned these calculations are mainly based on a prescribed neutral gas flux density impinging at the inner side of the wall and sticking there with a certain probability [9]. Depending on the energy spectrum implantation in the surface region [10] or backscattering [11] might be important. Besides these surface processes the volume processes, diffusion and trapping, are the basis for the buildup of the neutral gas inventory within the wall (Fig. 1). Therefore, a rigorous description of the neutral gas parameters in the wall requires that the parameters of the neutral gas background, e.g., the flux densities and the energy spactra, are known and that the surface and volume processes are taken into account. In general three hydrogen species are involved in these processes: deuterium and tritium as fuel and protium as minority species for ion cyclotron resonance heating. A synthesis of the

0021-9991/84 $3.00

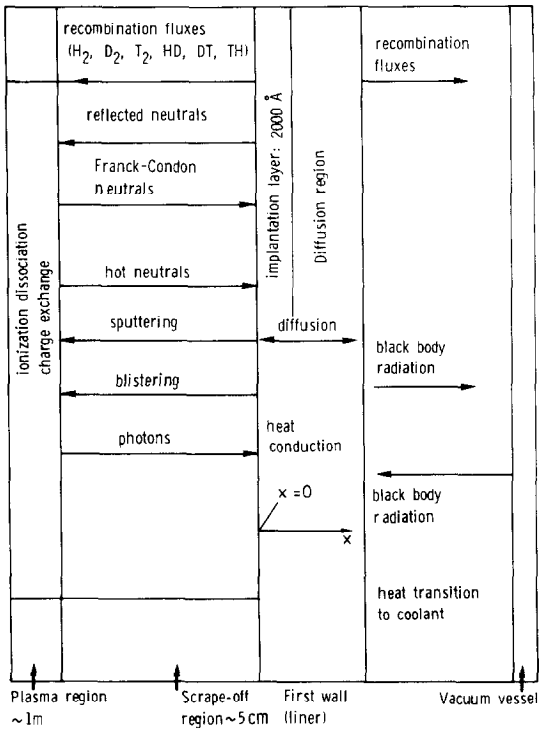

FIG. 1. Synthesis of possible first wall reactions.

first wall reactions is displayed in Fig. 1, which summarizes the interacting processes in the plasma region, in the scrape of region and in the first wall. The "wall energetics" are mainly determined by heat conduction, photon loading and heat transition to the coolant. The possible impurity production processes are sputtering, blistering and desorption. However, except for an estimate of the photon loading, the influence of the impurities on the plasma is neglected throughout this paper. The computation of the neutral gas parameters presumes that the plasma parameters are known, which follow from the operation scenario of the Tokamak reactor.

In the following a numerical modelling based on three codes, the "first wall module," "the neutral gas module" and "the plasma module," is presented and the main results concerning tritium permeation through the first wall of an INTOR-like device are given.

2. First Wall Module

This module (Fig. 2) accounts for the processes at the surface, in the surface region and in the bulk of the first wall. The heart is the part solving the diffusion equations for protium, deuterium and tritium. The recombination and implantation processes

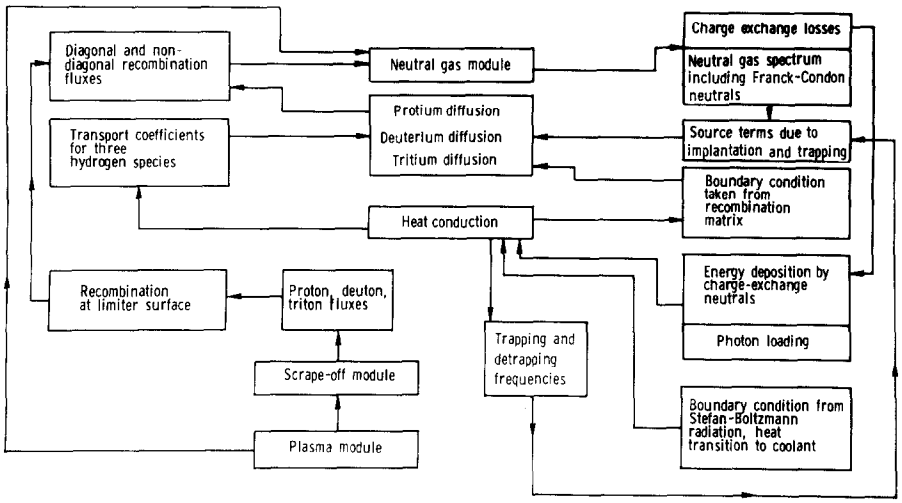

FIG. 2. Flow chart of the first wall module.

determine the boundary conditions and the source terms, respectively. The interaction with the neutral gas module arises because of the molecular fluxes coming from the wall and the charge exchange neutrals impinging at the first wall. The transport coefficients, the trapping and detrapping frequencies depend exponentially on the temperature profile emanating from the heat conduction law, the heat transition to the coolant, the energy deposition by charge exchange neutrals and the photon loading. The plasma module describing the time evolution of the plasma parameters interacts with the neutral gas module via the sources due to ionization and charge exchange.

2.1. *Diffusion*

The diffusion of the three hydrogen isotopes with the concentrations n_i is described by a set of three equations emanating from a generalization of Fick's law [5]:

$$\frac{\partial n_i(x,t)}{\partial t} = \frac{\partial}{\partial x}\left(D_i \frac{\partial n_i(x,t)}{\partial x}\right) + P_i + Q_i. \tag{2.1.1}$$

$i = 1$ stands for protium, $i = 2$ for deuterium and $i = 3$ for tritium. D_1, D_2, D_3 are the diffusion coefficients, t is the time, x is the distance from the inner surface (Fig. 1), P_i is the source term due to implantation and Q_i is the source term due to trapping.

The Soret effect [8] is neglected.

The Arrhenius equations for the diffusion coefficients read [5]

$$D_i = D_{0_i} \exp(-M_i/kT). \tag{2.1.2}$$

T is the absolute temperature, which is in general a function of x, and k is Boltzmann's constant. In case of protium and deuterium diffusing in SS the prefactors D_{0_i} and the migration energies [12, 13] are given by $D_{0_1} = 0.02\ \mathrm{cm}^2/\mathrm{sec}$, $D_{0_2} = 0.18\ \mathrm{cm}^2/\mathrm{sec}$, $M_1 = 0.57\ \mathrm{eV}$, $M_2 = 0.64\ \mathrm{eV}$.

The analogous values for tritium are not available. On theoretical grounds [5] one expects

$$D_{0_3} = \sqrt{(A_D/A_T)\, D_{0_2}}.$$

A_T and A_D are the atomic masses of tritium and deuterium, respectively. In addition the assumption $M_3 = M_2$ is made in the following. The equations are coupled by the boundary conditions accounting for the irradiation by Franck–Condon neutrals and the recombination

$$(-1)^K D_i \left(\frac{\partial n_i}{\partial x}\right)\Bigg|^K = \sum_{j=1}^{3} \alpha_{ij}^{(K)} n_i^{(K)} n_j^{(K)} - S_i^{(K)} \tag{2.1.3}$$

Here the indexing is done as follows:

As in Eq. (2.1.1) the lower indices i and j stand for the particle species and the upper index k denotes the surface, i.e., $k = 1$ for the outer surface and $k = 2$ for the inner surface of the wall (Fig. 1). The factor $(-1)^k$ accounts for the different directions of the concentration gradients at the two surfaces $n_i^{(k)}$, and $(\partial n_i/\partial x)|^k$ are the boundary values of the concentrations and of the concentration gradients. $\{\alpha_{i,j}^{(K)}\}$ is the recombination matrix. $S_i^{(k)}$ is the irradiation intensity by Franck–Condon neutrals, which are assumed to be partly deposited at the edge of the wall. The Arrhenius equations for the recombination coefficients characterized by the prefactors $\alpha_{0_{i,j}}$ and the activation energy $C_{i,j}$ read

$$\alpha_{i,j}^{(K)} = \alpha_{0_{i,j}} \exp(-C_{i,j}/kT^{(k)}). \tag{2.1.4}$$

$T^{(k)}$ is the temperature at the inner ($k = 2$) or at the outer surface ($k = 1$). Experimental data concerning the nondiagonal ($i \neq j$) recombination coefficients are not available. The data for the diagonal recombination of protium and deuterium reveal a considerable spread [13, 14]. Here the "σk_r-value" presented in [13] is used for the diagonal and nondiagonal recombination processes of protium, deuterium and tritium, i.e., we choose

$$\alpha_{0_{i,j}} = 1.42 \times 10^{-15}\ \mathrm{cm}^4/\mathrm{sec}$$
$$C_{i,j} = 0.78\ \mathrm{eV}.$$

2.2. *Heat Conduction*

The time evolution of the one-dimensional temperature T is described by

$$\frac{\partial T(x,t)}{\partial t} = \frac{\partial}{\partial x}\left(\chi \frac{\partial T}{\partial x}\right) + P_{cx} + P_{\Omega}. \tag{2.2.1}$$

The heat diffusivity χ reads

$$\chi = \lambda/(\rho c_v). \tag{2.2.2}$$

λ is the heat conductivity, ρ the density of the wall material and c_v the specific heat. For stainless steel we get $\chi = 0.063\ \mathrm{cm}^2/\mathrm{sec}$, and P_{cx} and P_Ω stand for the power densities due to the implantation of charge exchange neutrals and Ohmic heating which might be used for investigations at elevated temperatures. The boundary condition reads

$$\lambda \frac{dT}{dx}\bigg|^{(K)} = (-1)^K\,(q^{(K)} - f_b(T)^{(K)}). \tag{2.2.3}$$

$K = 1$ denotes the outer boundary, $K = 2$ the inner boundary, $q^{(k)}$ is the wall loading arising from the irradiation by Franck–Condon neutrals and by photons ($q^{(2)} = 0$). The function $f_b(T)$ accounts for the Stefan–Boltzmann radiation and the heat transition to the coolant

$$f_b(T) = \alpha(T - T_c) + \sigma\varepsilon(T^4 - T_c^4). \tag{2.2.4}$$

α is the heat transition coefficient, T_c the temperature of the coolant, σ the Stefan–Boltzmann constant and ε the emissivity of the wall. The environment of the wall is assumed to have the temperature of the coolant.

The heat transition coefficient α depends on Nusselt's number Nu, the heat conductivity λ and the characteristic lengths l and L of the structure containing the coolant [15] by the expression

$$\alpha = Nu\ \lambda/l.$$

Nusselt's number for turbulent streaming reads

$$Nu = 0.032 Re^{0.8} Pr^{0.37} (l/L)^{0.054}$$

in case of liquids and

$$Nu = 0.024 Re^{0.786} Pr^{0.45} (1 + (l/L)^{2/3})$$

in case of gases. Re is Reynolds number and Pr is Prandtl's number [15].

The coupled equations (2.1.1) and (2.2.1) are solved by the predictor–corrector method, which allows one to treat each of the four equations in principle independently. In this way the problem is reduced essentially to the inversion of a tridiagonal matrix (Section 2.5).

2.3. *Trapping*

The trapping centers within the wall cause the buildup of the trapped particle species. The evolution of the trapped particle density n_{T_j}, $j = 1, 2, 3$, is governed by the equations [5, 7]

$$\frac{\partial n_{T_j}(x, t)}{\partial t} = \mu_j n_j(x, t)\, n_e(x, t) - \nu_j n_{T_j}(x, t) \tag{2.3.1}$$

where the trapping coefficient μ_j and the detrapping frequency ν_j are given by [5]

$$\nu_j = \nu_0 \exp[-(M_j + E_T)/kT] \tag{2.3.2}$$

$$\mu_j = \frac{D_j}{\lambda_t^2 n_w}. \tag{2.3.3}$$

λ_t is the jump distance, n_w the concentration of the wall material, ν_0 the detrapping attempt frequency and E_T the binding energy of the traps. The concentration of the empty traps $n_e(x, t)$ reads

$$n_e(x, t) = n_{e_0}(x) - \sum_{j'} n_{T_{j'}}(x, t). \tag{2.3.4}$$

$n_e(x)$ is the concentration of the traps before irradiation. As at elevated temperatures the trapping and detrapping frequencies $\mu_j n_j$ and ν_j are several orders of magnitudes larger than the diffusion frequency D/a^2, and it is assumed here that on the diffusion time scale trapping is in equilibrium with detrapping. The analogous assumption is made in case of the coronal equilibrium, where the ionization and recombination frequencies are assumed to be much larger than the diffusion frequency of the plasma. The concentrations n_{T_j} are obtained from Eq. (2.3.1) by neglecting the time-derivative $\partial n_{T_j}/\partial t$. At low wall temperatures (room temperature), however, Eq. (2.3.1) must be fully taken into account. The system of linear equations describing the "trapping equilibrium" is solved simultaneously with the evolution equations (2.1.1) and (2.2.1).

2.4. *Implantation*

Two particle species emanate from the dissociation and charge exchange processes: the Franck–Condon neutrals in the temperature range of 3 to 5 eV and the "hot" neutrals emerging essentially with the plasma temperature. Whereas the Franck–Condon neutrals enter the wall at the surface and stick there with an unknown probability, the hot neutrals are partly backscattered in the surface region and partly deposited in the wall. This implantation takes place roughly in a surface layer of about 1000 Å and is described by energy-dependent deposition profiles; their analytic

representation is given in [5]. These profiles characterized by the average range [5] are normalized such that $\int_0^\infty dx H(x, E) = 1$.

2.5. *Computational Method*

The advantage of the predictor–corrector method [5] is that the coupled equations can be treated separately. The coupling of the equations is taken into account during the corrector steps. The differencing of the equations (2.1.1) is straightforward:

$$\frac{\hat{n}_{i,j}|_c^l - n_{i,j}}{\Delta t} = D_{i,j}(\tilde{T}_j)\frac{1}{2\Delta r_{j+1/2}}\left\{\frac{n_{i,j+1}-n_{i,j}}{\Delta r_{j+1}} - \frac{n_{i,j}-n_{i,j-1}}{\Delta r_j}\right.$$

$$\left. + \frac{\hat{n}_{i,j+1}|^l - \hat{n}_{i,j}|^l}{\Delta r_{j+1}} - \frac{\hat{n}_{i,j}|^l - \hat{n}_{i,j-1}|^l}{\Delta r_j}\right\} + P_{i,j} + Q_{i,j}. \quad (2.5.1)$$

An analogous equation emanates from Eq. (2.2.1). Here the additional index j is the space point index. The symbol $|^l$ denotes the lth corrector step, the roof the quantities after the time step Δt. Δ_{r_i} and $\Delta_{r_{i+1/2}}$ are the differences of the zone-centered and the boundary-centered grid. The tilde denotes the quantities at $t + \Delta t/2$. The predictor step ($l = 0$) is accomplished by setting $\tilde{T}_j = T_j$. During the corrector steps the relation $\tilde{T}_i|^l = \frac{1}{2}(\hat{T}_i|^{l-1} + T_i)$ is used.

To ensure numerical stability and accuracy the derivatives on the left-hand side of the boundary condition (2.1.3) and the expressions on the right-hand side of (2.1.3) are to be carfully centered in space and time. At the lth corrector step we get for the left-hand side of Eq. (2.1.3)

$$L^{(K)}|^l = \tfrac{1}{2} D_l[(\hat{n}_{i,m}|^l - \hat{n}_{im-1}|^l)/\Delta r_m + (n_{i,m} - n_{i,m-1})/\Delta r_m]. \quad (2.5.2)$$

Here the index m is given by

$$m = \begin{Bmatrix} N \\ 2 \end{Bmatrix} \quad \text{for the} \quad \begin{Bmatrix} \text{outer surface} \\ \text{inner surface} \end{Bmatrix}. \quad (2.5.3)$$

N is the node number of the zone-centered grid. The time centering of the right-hand side is done by the formulae

$$\tilde{A}^2|^l = \hat{A}|^l A \quad (2.5.4)$$

$$\widetilde{AB}\,|^l = \tfrac{1}{2}(\hat{A}|^l + A)\,\tilde{B}|^l. \quad (2.5.5)$$

At the lth corrector step the right-hand side of Eq. (2.1.3) reads

$$R_i^{(K)}|^l = \tfrac{1}{4}\alpha_{i,j}^{(K)}(n_{i,m} + n_{i,m-1})(\hat{n}_{i,m}|^l + n_{i,m-1}) + \sum_{j\neq i} \tfrac{1}{8}\alpha_{i,j}(\hat{n}_{i,m}|^l + \hat{n}_{i,m-1}|^l + n_{i,m} + n_{i,m-1}) \cdot (\tilde{n}_{j,m}|^l + \tilde{n}_{j,m-1}|^l) - S_i^{(K)}. \tag{2.5.6}$$

From the boundary conditions

$$L_i^{(K)}|^l = R_i^{(K)}|^l, \qquad K = 1, 2, \; i = 1, 2, 3 \tag{2.5.7}$$

and from Eq. (4.1) the elements of the tridiagonal matrix for each equation can be obtained which is to be inverted during the predictor and corrector steps. The correcting is finished if the quantities

$$R_i = \sum_j \left| \frac{\hat{n}_{i,j}|^l - \hat{n}_{i,j}|^{l-1}}{n_{i,j}} \right|, \qquad i = 1, 2, 3,$$
$$R_T = \sum_j \left| \frac{\hat{T}_j|^l - \hat{T}_j|^{l-1}}{T_j} \right| \tag{2.5.8}$$

are smaller than a prescribed accuracy parameter $\varepsilon = 10^{-2}$. If this condition cannot be satisfied after a prescribed number of corrector steps $l_{\max} = 5$, the time step is repeated with one-half of its original value.

2.6. *Consistency Checks*

Integration of Eq. (2.1.1) over the volume of the wall gives

$$\dot{N}_i = \sum_{k=1}^{2} \Big\} - \sum_{j=1}^{3} \alpha_{i,j}^{(k)} n_i^{(k)} n_j^{(k)} + S_i^{(k)} \Big\{ + A \int_0^d (P_i + Q_i)\, dx. \tag{2.6.1}$$

$\dot{N}_i$ is the time derivative of the particle content, A the area, and d the thickness of the wall. Integrating Eq. (2.6.1) over the time yields

$$N_i(t) = \int_0^t R\, dt + N_i \qquad (t = 0) \tag{2.6.2}$$

where R is the RHS of Eq. (2.6.1). The LHS of Eq. (2.6.1) and (2.6.2) can be computed from the spatial and temporal evolution of the particle densities $n_i(x)$ as well, resulting in $\bar{\dot{N}}_i$ and $\bar{N}_i$. The relative deviations

$$d_2 = |N_i(t) - \bar{N}_i(t)|/N_i(t) \tag{2.6.3}$$

and

$$d_1 = |\dot{N}_i(t) - \bar{\dot{N}}_i(t)|/S_{\text{ab}} \tag{2.6.4}$$

stay below 10^{-4} and 10^{-2}, respectively, in all calculations mentioned in Section 5.

S_{ab} is the sum over the absolute values of the terms in the RHS of Eq. (2.6.1). d_1 and d_2 depend essentially on the accuracy parameter ε and the prescribed upper limit Δt_{max} of the time step Δt. Δt_{max} ranges between 20 and 100 sec in the examples given in Section 5.

3. Neutral Gas Module

The ions, H^+, D^+, T^+, impinging at the limiter (or divertor plate), are assumed to be neutralized completely thereby neglecting backscattering. The atoms are partly deposited in the edge region of the limiter material recombining to "diagonal" and "nondiagonal" molecules H_2, D_2, T_2, HD, HT and DT and are partly backscattered. The fraction of the atoms diffusing into the limiter (divertor plate) material can be estimated to be negligibly small (about $1\,0/_{00}$ of the recombination flux). Acording to Eq. (2.1.3) the flux balance at the surface of the metal reads

$$\begin{aligned}
\left.\frac{d\phi_{H^+}}{df}\right|_S &= \alpha_{11} n_H^2 + \alpha_{12} n_H n_D + \alpha_{13} n_H n_T \\
\left.\frac{d\phi_{D^+}}{df}\right|_S &= \alpha_{21} n_D n_H + \alpha_{22} n_{D^2} + \alpha_{23} n_D n_T \\
\left.\frac{d\phi_{T^+}}{df}\right|_S &= \alpha_{31} n_T n_H + \alpha_{32} n_T n_D + \alpha_{33} n_{T^2}
\end{aligned} \tag{3.1}$$

and

$$\left.\frac{d\phi_{H^+}}{df}\right|_S, \quad \left.\frac{d\phi_{D^+}}{df}\right|_S \quad \text{and} \quad \left.\frac{d\phi_{T^+}}{df}\right|_S$$

are the flux densities of protons, deutons and tritons, respectively, hitting the surface element df of the limiter and sticking in the surface region. n_H, n_D, n_T are the densities of protium, deuterium and tritium in this region of the limiter.

Within the Monte-Carlo approach described below the flux densities of the backscattered atoms are computed by sampling from a maxwellian having the temperature $T_i = 60$ eV and by employing one of the backscattering models described in Section 3.4. The choice $T_i = 60$ eV is roughly justified by the sheath potential in fromt of the limiter. In this approach the limiter geometry which is in general three dimensional is not specified. To be consistent within the one-dimensional models used here throughout it is assumed instead that the ion fluxes and the resulting molecular fluxes are uniformly distributed over a toroidal surface going through the limiter edge. Hence we have, e.g., for the protons,

$$\left.\frac{d\phi_{H^+}}{df}\right|_S = \phi_{H^+}/F_{tor};$$

F_{tor} is the area of torus surface. ϕ_{H^+} is the total proton flux sticking at the limiter. The quadratically coupled system of Eqs. (3.1) is solved by Newton iteration. From the densities n_H, n_D, n_T the molecular fluxes are derived, emanating from the limiter and evoking the molecular effects [16].

A treatment of the neutral gas transport in cylindrical plasmas by the Monte-Carlo algorithm including nonanalogue methods to reduce the variance has been described already in [11]. However, as only the atomic species H, D and T are taken into account, the flux of Franck–Condon neutrals arising from the dissociation of the molecular species cannot be computed. Here the molecules are launched and tracked by a similar method as in the case of the atoms [17]. The treatment of the molecular processes is described in Section 3.2, and the atomic processes accounted for are the "diagonal and nondiagonal" charge exchange, electron and ion impact ionization. The rate coefficients are the same as in Ref. [11], as far as charge exchange and electron impact ionization are concerned. The rate coefficient for ion impact ionization is computed from the fit for the corresponding cross section in Ref. [18].

Besides bias sampling (suppression of ionization) another nonanalogue method (Section 3.3) and an efficient scoring technique (Section 3.1) are employed to reduce the variance. The spectrum of the charge exchange and Franck–Condon neutrals is obtained by calculating the Monte-Carlo particle's probability to escape within a prescribed energy range after each collision. In this calculation it is presupposed that the particle escapes without further collision. The atoms backscattered at the wall and the molecules born there due to recombination are tracked in the same way as those arising from the limiter. Details of the backscattering model are given in Section 3.4.

The number of Monte-Carlo particles ($N_M \approx 5 \cdot 10^3$) is chosen such that the maximum statistical error of the spectrum is about 10% for $E < 2$ keV, around 30% in the range 2 keV $< E <$ 4 keV and roughly 60% in the high-energy range (4 keV $< E <$ 6 keV). The maximum statistical error of the fluxes obtained by integration over the spectra of the different particle species is about 1%.

3.1. *Scoring*

The scoring of the macroscopic quantities (densities, pressure, gain and loss terms) is done by the tracklength estimator, the collision estimator or by a linear combination of both. In the first case the contribution of each particle history is calculated by computing the time intervals spent in the mesh cells of the grid [17], in the second by summing up the contributions of the collisions in each mesh cell, and in the third the benefit of the estimators' complementary behaviour in regions with strongly different neutral gas densities is employed to reduce the variance. Although the code is capable of using a two-dimensional or three-dimensional mesh the one-dimensional grid has been used throughout because of the same reasons mentioned Section 3.

3.2. *Molecular Processes*

The molecular processes accounted for in case of protium are summarized in Table I: molecular dissociation (1), molecular dissociative ionization (2), direct molecular

TABLE I

Molecular Protium Processes

(1)	$e + H_2^0 \rightarrow 2H^0 + e$
(2)	$e + H_2^0 \rightarrow H^0 + H^+ + 2e$
(3)	$e + H_2^0 \rightarrow H_2^+ + 2e$
(4)	$e + H_2^+ \rightarrow 2H^0$
(5)	$e + H_2^+ \rightarrow H_0 + H^+ + e$
(6)	$e + H_2^+ \rightarrow 2H^+ + 2e$

ionization (3), molecular ion dissociative recombination (4), molecular ion dissociative excitation (5) and molecular ion dissociative ionization (6). Analogous processes hold for the molecules D_2, T_2, HD, HT and DT. The rate coefficients for the reactions (1)–(6) are computed directly from the fits given in [19]. The same coefficients are used for the processes involving the molecules just mentioned. The different masses M_i ($i = 1, 2, \ldots, 6$) enter the expressions for molecular velocities v_{m_i}

$$v_{m_i} = \sqrt{\frac{3kT_R}{m_i}} \tag{3.2.1}$$

only. All molecules are launched with room temperature T_R. The tracklength of the molecules is sampled as in the case of the atoms [11] from the distribution

$$d(l) = \frac{1}{\lambda(l)} \exp\left[-\int_0^{l'} \frac{dl'}{\lambda(l')}\right] \tag{3.2.2}$$

where λ is the mean free path length. In the specific case here the absorption is due to the processes (1)–(3) in case of H_2 and due to the analogous processes in case of the other molecules. It is assumed that the molecular ions decay immediately, if the molecules are stopped by reaction (3). The mean number of secondary particles (H^0, D^0, T^0) generated thereby is

$$\mu = \frac{1/\lambda_1 + 1/\lambda_2 + \alpha/\lambda_3}{1/\lambda_t} \tag{3.2.3}$$

and

$$\lambda_t = \lambda_1 + \lambda_2 + \lambda_3 \tag{3.2.4}$$

is the mean free path length of the six molecular species. α accounts for the processes (4)–(6):

$$\alpha = \frac{2/\lambda_4 + 1/\lambda_5}{1/\lambda_4 + 1/\lambda_5 + 1/\lambda_6}. \tag{3.2.5}$$

The index i in λ_i refers to Table I. μ is introduced into the Monte-Carlo algorithm as a weight-correcting factor.

3.3. *Nonanalogue Method*

The main disadvantage of the distribution (3.1.1) is its roughly exponential decrease with increasing distance from the source point. This implies a high variance at large distances if a simple analogue method is used. To avoid this splitting and Russian roulette are applied [11]. A generalization of this technique not depending on prescribed splitting surfaces and resorting to a general "importance function" $\bar{I}(\mathbf{r}, \mathbf{v})$ instead is given in [20] for deep penetration problems in (fission) reactor physics; $(\mathbf{r}, \mathbf{v})$ denotes a point in ordinary and velocity space.

Here the distribution (3.2.1) is replaced by the product $\bar{d}(l) = d(l)\, I(l)$ in which $I(l)$ is a function (analogous to $\bar{I}$) mainly effecting that the tracklengths for (Monte-Carlo) particles travelling away from the sourcepoint become longer than those in the simple analogue case; for the particles moving in the opposite direction the contrary holds.

The weight and the mean particle number are adjusted in case of a collision such that unbiased results are obtained. The specific expression for $I(l)$ reads

$$I(l) = \exp\left[-\frac{\bar{l}(l)}{l_0} + \frac{\bar{l}_I}{l_0}\right]. \tag{3.3.1}$$

$\bar{l}$ is the distance of the point A_l on the particle track from a prescribed point A_I, where the maximum statistical error is supposed to occur (i.e., the plasma center). l_0 is a prescribed length roughly equal to the e-folding length of the variance in the analogue case; this variance decreases strongly with decreasing distance from the source of the neutral particles. $\bar{l}_I = \bar{l}(0)$ is the distance of the source point S from A_I (Fig. 3). Sampling from the (not normalized) distribution $\bar{d}(l)$ is achieved by splitting the particle in the average into $\nu = I(l_c)$ particles if $\bar{l}_I > \bar{l}(l_c)$ or by deleting it with the probability $p = 1 - I(l_c)$ if $\bar{l}_I \leqslant \bar{l}(l_c)$; l_c is a specific value of the tracklength l sampled from the distribution (3.1.1). In either case the weight of the released particle(s) is (are) multiplied by $1/I(l_c)$. In the one-dimensional approach used here this technique is approximately equivalent to splitting and Russian roulette. In two-dimensional calculation, e.g., with radial and poloidal resolution in case of the toroidal limiter mentioned in Ref. [17], the method improves the efficiency of the neutral gas module (maximum variance/CPU-time) by a factor of 100.

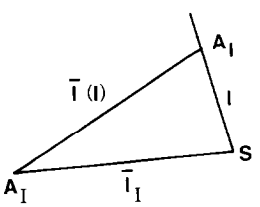

FIG. 3. Geometry underlying the nonanalogue method.

3.4. *Backscattering*

The backscattering can be described in general by sampling from the three-dimensional distribution $\omega_{E,\theta}(E', \theta', \varphi')$ depending on the energy of the incident, the energy of the backscattered, the polar angle of the incident, and the polar and azimuthal angles of the backscattered particle, E, E', θ, θ', φ', respectively. (See Fig. 4.) The data obtained experimentally [21–23] or theoretically [24, 25] concern the number-backscattering coefficient

$$R_p(E) = \int_0^{\infty} \int_0^{\pi/2} \int_0^{2\pi} \omega_{E,(\theta=0)}(E', \theta'\varphi')\, dE' \sin\theta'\, d\theta'\, d\varphi', \tag{3.4.1}$$

the energy-backscattering coefficient

$$R_E(E) = \int_0^{\infty} \int_0^{\pi/2} \int_0^{2\pi} E'\omega_{E,(\theta=0)}(E', \theta', \varphi') \sin\theta'\, d\theta'\, d\varphi'\, dE/(ER_p(E)) \tag{3.4.2}$$

and the distribution ω itself [25]. They reveal a significant spread, e.g., the important number-backscattering for the Franck–Condon neutrals obtained by extrapolation from Ref. [21] is 1 in case of protium and that from Ref. [22] is 0.5. For deuterium the analogous numbers are 1 and 0.85, respectively. Measurements concerning the angular and the energy dependences in the range $10^{-3}\,\text{eV} < E < 100\,\text{eV}$ are not available. At very low energies $E \lesssim 10^{-3}\,\text{eV}$, however, the measured backscattering coefficient vanishes [4]. Therefore a simple extrapolation of the data [21–23] might lead to an overestimation of the Franck–Condon neutrals' backscattering. To avoid

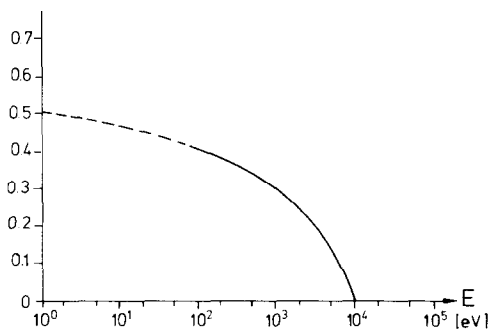

FIG. 4. Particle backscattering coefficient.

account for the energy distribution of the backscattered particles [21] sampling from the following expression for ω is implemented in the neutral gas module:

$$\omega_{E,\theta}(E', \theta', \varphi') = R_{p_1}(E, \theta)\, R_{E_1}(E, \theta; E')\, S(\theta; \theta', \varphi'). \tag{3.4.3}$$

$R_{p_1}(E, \theta)$ describes the dependence of the particle backscattering coefficient on the incident angle. The expression

$$R_{p_1}(E, \theta) = 1 - (1 - R_p(E)) \cos^{l_p}(\theta) \tag{3.4.4}$$

accounts approximately for the results obtained by the MARLOWE-code, if $l_p = 1$ [24, 26]. The quantity R_{E_1} is related to the generalized energy backscattering coefficient $R_{E_2}(E, \theta)$ defined by the LHS of Eq. (3.4.2) without restriction in θ. The relation reads

$$R_{E_2}(E, \theta) = \int dE' E' R_{E_1}(E, \theta; E')/E. \tag{3.4.5}$$

The expression

$$R_{E_2}(E, \theta) = 1 - (1 - R_E(E)) \cos^{l_E}(\theta) \tag{3.4.6}$$

accounts again approximately for the angular dependence of R_{E_2} computed by MARLOWE, if $l_E = 0.5$ [26].

The choice for $R_{E_1}(E, \theta; E')$ used here reproduces the coefficient (3.4.6) and the energy distribution of the backscattered particles for normal incidence

$$R_{E_1}(E, (\theta = 0), E'') = R_B(E, E'') \tag{3.4.7}$$

in Ref. [21]. We note that the transformed distribution $\bar{f}$ of $y = f(x)$ with x having the distribution $g(x)$ reads [27]

$$\bar{f}(y) = \frac{g(f^{-1}(y))}{f'(f^{-1}(y))}. \tag{3.4.8}$$

f^{-1} is the inverse function of $f(x)$ and the prime denotes the derivative. In $R_B(E, E'')$ we choose a transformation $E' = f(\theta, E; E'')$ accounting for the oblique incidence. Hence $R_{E_1}(E, \theta; E'')$ reads

$$R_{E_1}(E, \theta; E') = R_B[E, f^{-1}(\theta, E; E')]/f'(f^{-1}(E')). \tag{3.4.9}$$

The relation (3.4.6) holds if

$$f(\theta, E; E'') = E - (E - E'') \cos^{l_E}(\theta). \tag{3.4.10}$$

Random numbers E from the distribution (3.4.9) can be obtained by sampling E'' from $R_B(E; E'')$ and by transforming E'' to E' by Eq. (3.4.10).

$R_p(E)$ is taken from Ref. [21] as well, so that the choice $l_p = l_E = 0$ results in the backscattering model presented there.

The distribution $S_\theta(\theta', \varphi')$ describes the transition from specular reflection to diffuse reflection according to Ref. [28]. The cosine distribution can be used instead as an option.

To show the sensitivity of the neutral gas spectra, the total emerging, backscattered and sticking fluxes with respect to different backscattering models in Section 5, the results for $l_p = 1$, $l_E = 0.5$ and S_θ according to Ref. [28] are compared with those for $l_p = l_E = 0$ and $S_\theta \sim \cos(\theta')$.

3.5. *Consistency Checks*

Because of stationarity the sum of the particle gains ϕ_g equals the sum of the particle losses ϕ_l. The same holds for the power gains and losses χ_g and χ_l respectively. ϕ_g and ϕ_l read

$$\phi_g = \phi_i + \phi_b + \phi_r + \phi_0$$
$$\phi_l = \phi_j + \phi_0 + \phi_m.$$

ϕ_i is the total atomic and molecular influx.
ϕ_b is the backscattered atomic flux.
ϕ_r is the molecular flux due to recombination at the wall.
ϕ_a is the atomic gain by dissociation.
ϕ_j is the atomic ionization loss.
ϕ_0 is the total atomic and molecular flux leaving the plasma.
ϕ_m is the molecular loss by dissociation.

The variance inherent to the Monte-Carlo method causes the main deviation between ϕ_g and ϕ_l. Due to the variance reduction techniques and the sufficiently high number of Monte-Carlo particles $N_M = 5 \cdot 10^3$ the relative deviation

$$d_p = |(\phi_g - \phi_l)| \phi_g|$$

stays below 1%. χ_g and χ_l read

$$\chi_g = \chi_i + \chi_{cx} + \chi_b + \chi_a$$
$$\chi_l = \chi_0 + \chi_j.$$

χ_i is the power released at the source (limiter).
χ_{cx} is power gain by charge exchange.
χ_b is power gain by backscattering.
χ_a is power carried by the atoms due to dissociation.
χ_0 is power deposited at the wall.
χ_j is power loss by ionization.
The relative deviation

$$d_E = |(\chi_g - \chi_i)/\chi_g|$$

stays below 2%.

4. Plasma Module

As mentioned in Fig. 1 the ions of the plasma background act as a source for the charge exchange neutrals, and the electrons in the boundary region provide the energy for the dissociation processes. The description of the plasma background is based on one-dimensional evolution equations for the particle, energy and magnetic field transport given elsewhere [30, 31] in detail. The heart of the plasma module is the part solving the diffusion-type equations for the electron temperature, the ion temperature, and the proton, deuton and triton densities by the predictor–corrector method [5]. The energy source terms due to Ohmic, beam and RF heating and ionization and charge exchange are obtained from radial dependence of the poloidal field, the beam heating module [32], a simplified RF-heating model and the neutral particle module, respectively; several models are available for the computation of the transport coefficients. Here a simple model [33] is chosen for the perpendicular transport described by the diffusion coefficient D and by the electron and the ion heat diffusivities χ_e, and χ_i:

$$\begin{aligned} \chi_e &= \frac{5 \cdot 10^{17}}{n_e \,\mathrm{cm}^3} \frac{\mathrm{cm2}}{\mathrm{sec}} \\ \chi_i &= f(v_i^*)\, q^2 \rho_i^2 \nu_{ii} \\ D/\chi_e &= 0.25. \end{aligned} \tag{4.1}$$

The function f depending on the collisionality v_i^* is given in [34]; q is the safety factor, ρ_i the ion larmor radius and ν_{ii} the ion–ion collision frequency.

Instead of the neoclassical inward flow [34] the phenomenological inward flow term advanced by Engelhardt *et al.* [35] is used,

$$\phi_{i_r}(r) = -\, n(r) \frac{2D_\perp r}{r_{\mathrm{LIM}}^2} \tag{4.2}$$

r_{LIM} is the radius of the limiter edge.

5. Results

As a specific example the code is applied to the first wall of an INTOR-like device. The computing facility is an IBM 3033 V 12 computer interacting with an MVS (multiple virtual storage)–Batch system.

In addition to the modelling made above the following approximations aiming mainly at a reduction of the necessary computer time are employed:

1. The fluxes penetrating into the wall are small compared to those being recycled at the wall, so that in spite of the losses to the wall 100% recycling can be assumed.

2. In the time between two discharges the hydrogen species are frozen in because of the temperature decrease in the wall between the shots. This means that instead of the intermitting irradiation current ϕ_{int} the time average of this current

$$\bar{\phi} = D\phi_{int} \tag{5.1}$$

can be used. $D = \tau_p/(\tau_p + \tau_d)$ is the duty cycle, τ_p the pulse duration and τ_d the time interval of the pause (dwell). In the following $D = 3/4$ has been assumed throughout.

The second approximation leads to a considerable reduction of the computer time needed to calculate the time evolution of the hydrogen inventory during the Tokamak operation time. A comparison between a run with intermitting irradiation current ($\tau_p = 900$ sec, $\tau_d = 300$ sec) and a run with constant current, both with prescribed wall temperature $T_w = 500°C$, shows that the CPU time is reduced from 1085 sec to 191 sec. The operation time was 9600 sec in either case. The reason for the high value in case of the intermitting irradiation is the reduction of the time step necessary to obtain a constant prescribed accuracy ε (Section 2.5) at the beginning of the irradiation phase and of the pause, when the density near the surface layer changes rapidly. The specific values of τ_p and τ_d are chosen to show the impact of an intermitting current on the CPU time only. Realistic values, e.g., $\tau_p = 75$ sec, $\tau_d = 25$ sec, result in CPU times estimated to be roughly three hours for the example given above. An operation time of 10^6 sec necessary at low wall temperatures to reach saturation of the hydrogen inventory results in a much higher CPU time. In case of the examples discussed below and summarized in Table II the assumption (5.1) leads to a maximum CPU time of 960 sec.

The calculations are based essentially on the INTOR data specified in [36]: minor radius $a = 1.50$ m, major radius $R_0 = 5.30$ m, plasma current $I_p = 6.4$ MA, toroidal field $B_t = 5.5$ Tesla, initial mean deuton density $n_{D_i} = 7 \cdot 10^{13}/cm^3$, mean triton density $n_T = 7 \cdot 10^{13}/cm^3$, mean proton density $n_H = 7 \cdot 10^{12}/cm^3$ and mean ion and

TABLE II

Tritium Permeation Rates (kCi/day) and Tritium Inventory (kCi)

Coolant	T_w (°C)	ϕ_{T_2} (kCi/day)	ϕ_{HT} (kCi/day)	ϕ_{DT} (kCi/day)	$\sum\phi$ (kCi/day)	I_T (*kCi*)	T_r (sec)
Water $T_c = 100°C$	242	5.76	2.31	7.56	13.5	574	$6 \cdot 10^5$
Water $T_c = 200°C$	319	22.7	909	26.3	49.9	219	$7.5 \cdot 10^4$
Helium $P_e = 30$ bar	452	62.4	124	73.8	137	56.4	$9 \cdot 10^3$
Helium $P_e = 20$ bar	568	139	460	154	298	25.9	$3.3 \cdot 10^3$

electron temperature during the flat top phase $\langle T_e \rangle = \langle T_i \rangle = 10$ keV. The operation scenario demonstrated by means of the time evolution of the ion temperature (Fig. 5) is as follows: between $t = 0$ sec and $t = 1$ sec the plasma is heated by neutral injection heating only (beam power $p_b = 20$ MW; maximum beam energy $E_b = 175$ keV; injected species: deuterium). At $t = 1$ sec ion cyclotron resonance heating is turned on in addition (ICRH power $P_i = 30$ MW). As soon as the mean ion temperature reaches 10 keV the temperatures become feedback controlled thereby maintaining essentially the mean values $\langle T_e \rangle$ and $\langle T_i \rangle$ during the burn phase.

The fluxes of ionized protons, deutons and tritons hitting the limiter at $t = 7.5$ sec are

$$\phi_{H^+} = 2.6 \text{ kA}, \qquad \phi_{D^+} = 34.9 \text{ kA}, \qquad \phi_{T^+} = 26.2 \text{ kA} \tag{5.2}$$

respectively. Although the initial densities n_{D_i} and n_{T_i} are equal, the deuton flux is somewhat higher than the triton flux because of neutral injection heating, which enhances the deuton density.

The fluxes (5.2) are employed in the neutral gas module. The parameters of the backscattering model are $l_E = l_p = 0$; $S(\theta; \theta'\varphi')$ is assumed to be proportional to $\cos(\theta')$ (rough walls). Other parameters are chosen later on to show their influence on the neutral gas parameters.

The atomic and molecular fluxes due to backscattering and recombination at the limiter are

$$\begin{aligned} \phi_H &= 1.5\ kA, & \phi_D &= 22.0 \text{ kA}, & \phi_T &= 16.4 \text{ kA} \\ \phi_{H_2}|_L &= 32 \text{ A}, & \phi_{D_2}|_L &= 7 \text{ kA}, & \phi_{T_2}|_L &= 4.0 \text{ kA} \\ \phi_{HD}|_L &= 1.0 \text{ kA}, & \phi_{HT}|_L &= 0.8 \text{ kA}, & \phi_{DT}|_L &= 10.7 \text{ kA}. \end{aligned} \tag{5.3}$$

The fluxes (5.3) are the starting point for the calculation of the neutral gas parameters. The main result is the spectrum of the emerging neutrals consisting of

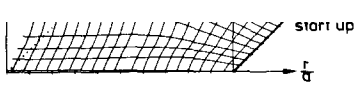

FIG. 5. Time evolution of the ion temperature. $T_{i_{max}} = 20$ keV, $T_{max} = 10$ sec, $a = 150$ cm.

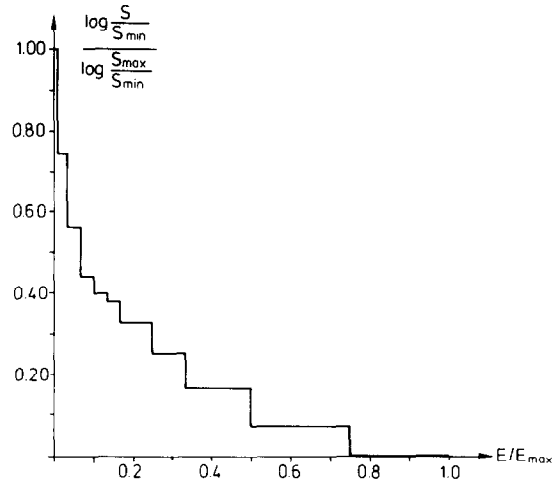

FIG. 6. Spectrum of the emerging tritium atoms ($l_p = l_E = 0$). $S_{max} = 647$ A/eV, $S_{min} = 4.7 \cdot 10^{-3}$ A/eV, $E_{max} = 6$ keV.

charge exchange and Franck–Condon neutrals. The spectrum of the tritium atoms is shown in Fig. 6. It is strongly peaked between 0 and 50 eV because of the Franck–Condon neutrals. The fraction of the neutrals in this energy interval is about 85%. The spectrum of the backscattered neutrals is displayed in Fig. 7. Here the maximum is about half as large as the maximum in Fig. 9. The sums of the charge exchange and the Franck–Condon fluxes hitting the wall are

$$\phi_{cx_H} = 3.7 \text{ kA}, \qquad \phi_{cx_D} = 35.6 \text{ kA}, \qquad \phi_{cx_T} = 37.4 \text{ kA}. \tag{5.4}$$

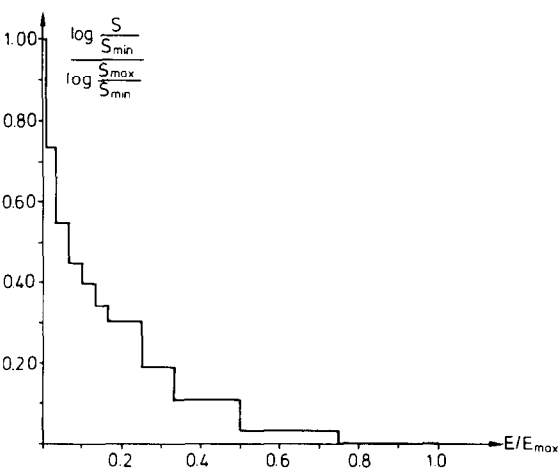

FIG. 7. Spectrum of the backscattered tritium atoms ($l_p = l_E = 0$). $S_{max} = 334$ A/eV, $S_{min} = 6.7 \cdot 10^{-5}$ A/eV, $E_{max} = 6$ keV.

A comparison with the ionic fluxes (5.2) shows that they are even larger than those in contrast to the results obtained from neutral gas models neglecting backscattering [31]. The reason is multiple backscattering of the same particle at the wall. The atomic fluxes backscattered from the wall read

$$\phi_{r_H} = 1.70\,\text{kA}, \qquad \phi_{r_D} = 17.1\,\text{kA} \qquad \text{and} \qquad \phi_{r_T} = 17.9\,\text{kA}.$$

Finally, the time-averaged flux densities (5.1) deposited into the lattice of the metal turn out to be

$$\begin{aligned} \overline{\phi_{d_H}} &= 2.90\ 10^{15}\ \text{cm}^{-2}\,\text{sec}^{-1}, \qquad \overline{\phi_{d_D}} = 2.59\ 10^{16}\ \text{cm}^{-2}\,\text{sec}^{-1} \\ \overline{\phi_{d_T}} &= 2.84\ 10^{16}\ \text{cm}^{-2}\,\text{sec}^{-1}. \end{aligned} \tag{5.5}$$

The atoms sticking in the lattice of the metal diffuse primarily to the surface (only about $1\,{}^{0}/_{00}$ diffuses to the downstream side) and recombine there. The recombination fluxes are

$$\begin{aligned} &\phi_{H_2}|_W = 31\ \text{A}, \qquad \phi_{D_2}|_W = 6.0\,\text{kA}, \qquad \phi_{T_2}|_W = 3.3\,\text{kA} \\ &\phi_{HD}|_W = 0.90\,\text{kA}, \qquad \phi_{HT}|_W = 0.67\,\text{kA}, \qquad \phi_{DT}|_W = 8.9\,\text{kA}. \end{aligned} \tag{5.6}$$

They are somewhat smaller than those recombining at the limiter although the fluxes (5.4) are larger than the fluxes (5.2). The reason is the rather high backscattering coefficient of the Franck–Condon neutrals. The calculation is repeated with the parameters $l_E = 0.5$, $l_P = 1$ and $S(\theta; \theta'\varphi')$ taken from Ref. [28]. The main fluxes are now

$$\begin{aligned} \phi_{cx_D} &= 58.7\,\text{kA}, & \phi_{cx_T} &= 51.6\,\text{kA}, \\ \phi_{r_D} &= 46.0\,\text{kA}, & \phi_{r_T} &= 40.0\,\text{kA}, \\ \bar{\phi}_{d_D} &= 1.82\ 10^{16}\ \text{cm}^{-2}\,\text{sec}^{-1}, & \bar{\phi}_{d_T} &= 1.68\ 10^{16}\ \text{cm}^{-2}\,\text{sec}^{-1}. \end{aligned}$$

The deuterium and tritium charge exchange fluxes become higher by factors of 1.64 and 1.37, respectively. The analogous numbers in case of the reflected fluxes are 2.69 and 2.23. The reasons for these significant enhancements are essentially twofold:

1. The particle backscattering coefficient is higher in the average and especially large for particles with grazing incidence originating mainly from the boundary region.

2. The specular reflection described by the distribution $S(\theta; \theta', \varphi')$ tries to keep particles with grazing incidence in the boundary region. This amplifies the effect just mentioned.

The sticking flux densities are decreased by 30% in case of deuterium and by 40% in case of tritium. This change is small compared to the change of the backscattered fluxes because both the charge exchange and the backscattered fluxes are increased.

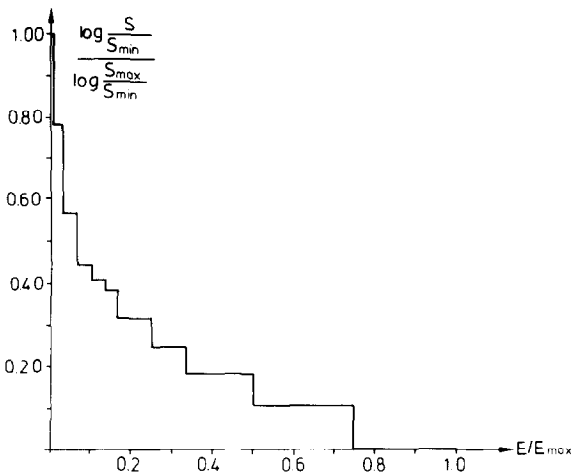

FIG. 8. Spectrum of the emerging tritium atoms ($l_p = 1$, $l_E = 0.5$). $S_{max} = 870$ A/eV, $S_{min} = 1.7 \cdot 10^{-3}$ A/eV, $E_{max} = 6$ keV.

Fig. 8 shows the spectrum of the tritium atoms generated by charge exchange and the dissociation processes. In the low-energy range the spectral density is about 30% higher than that in Fig. 6. At high energies the spectral densities of Figs. 6 and 8 agree within the error limits due to the variance, because hot neutrals hit the wall in general with small polar angle. In case of the backscattered tritium atoms (Fig. 9) the spectral density is roughly twice as high as that in Fig. 7, if the energy is small. The reasons are the same as in case of the backscattering fluxes.

The more sophisticated backscattering model changes the fluxes and their spectra significantly. Because of the rough walls, however, the sticking flux densities (5.5) are

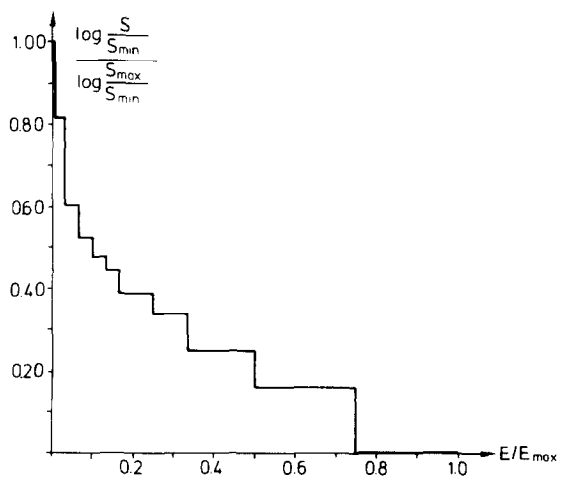

FIG. 9. Spectrum of the backscattered tritium atoms ($l_p = 1$, $l_E = 0.5$). $S_{max} = 710$ A/eV, $S_{max} = 2.7 \cdot 10^{-5}$ A/eV, $E_{max} = 6$ keV.

assumed to be a more realistic basis for the computation with the first wall module. These fluxes and their spectral distribution are used for the source terms in Eqs. (2.1.1).

The wall's thickness is assumed here to be 0.5 cm. The effective length of the structure containing the coolant is chosen to be $l = 2$ cm. The wall's area is that of the outermost flux surface (325 m^2). The estimate of the wall loading is 100 MW [37]. This loading is assumed to be distributed uniformly over the surface of the first wall, because calculations with a modified version of the BALDUR-code [38] show that the main part of the power deposited in the plasma is lost by line-radiation; impurities due to charge exchange sputtering and due to ion impact are included in these calculations. In case of a pump limiter design most of the charge exchange power is deposited on the limiter face [29] thus effecting a nonuniform loading in principle. However, the charge exchange loading is small compared to the radiation loading (~5%).

The streaming velocity of the coolant is chosen to be $v_{st} = 20$ m/sec in case of helium cooling and $v_{st} = 0.5$ m/sec in case of water cooling. The helium temperature is 100°C, and the pressure 20 or 30 bar.

Table II gives an overview of the fluxes of radioactivity (Curie/day), the tritium content I_T (Curie) and the rise time of the radioactivity due to the tritium diffusion; ϕ_{D_2}, ϕ_{HT} and ϕ_{DT} are the fluxes of T_2, HT and DT molecules, produced by recombination. Four cases characterized by the parameters of the coolant are listed. The table shows that at $T_w = 242$°C the total permeation rate is rather low (13.5 kCi/day), whereas the tritium content, to be released after shut down, is rather

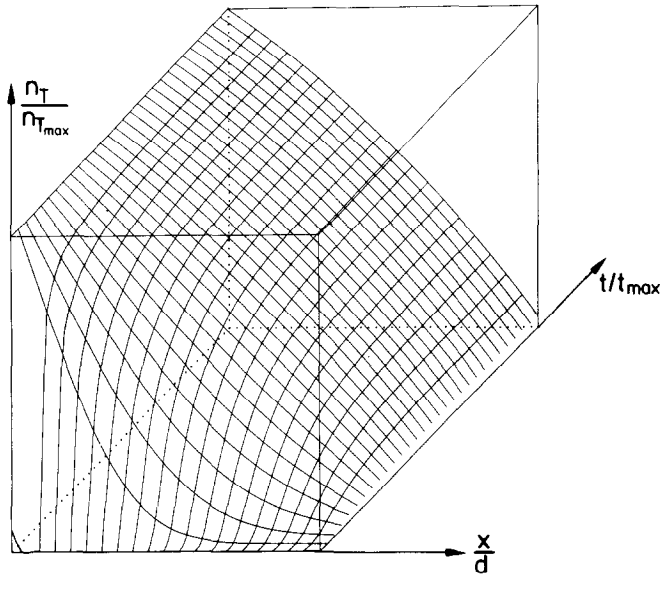

FIG. 10. Time evolution of the tritium density. $n_{T_{max}} = 576 \cdot 10^{17}$, $t_{max} = 10^4$ sec, $d = 0.5$ cm.

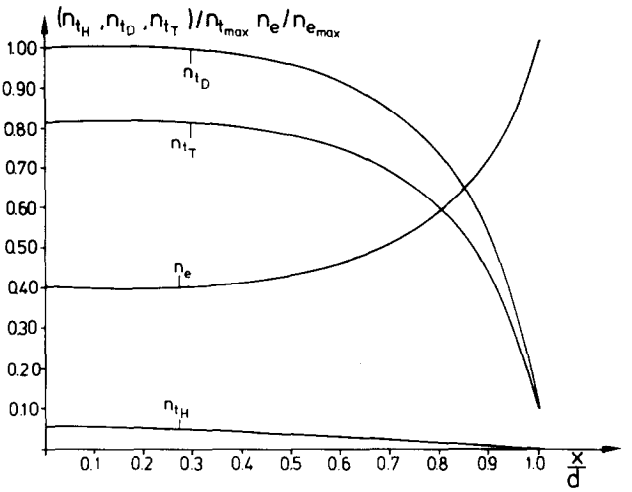

FIG. 11. Density of the trapped particle species. $n_{t_{max}} = 782 \cdot 10^8$, $n_{e_{max}} = 213 \cdot 10^9$, $d = 0.5$ cm.

high (574 kCi). The radioactivity rise time is $T_r = 6 \cdot 10^5$ sec. Due to the exponential dependence of the diffusion coefficient on the temperature the permutation rate at 568°C is higher by a factor of 20 and the tritium content is lower by a factor of 22. In case of water cooling, the mean wall temperature $T_w = 242$°C deviates from the temperature of the coolant by about 140°C, whereas in case of helium cooling the mean wall temperature is much higher than the helium temperature.

The main result is that a low permeation rate is to be paid by a large tritium content if the stationary state of the tritium inventry is reached. To avoid this, the rise time of the radioactivity should be smaller than the operation time of the reactor.

Figure 10 displays the time evolution of the tritium density in the metal, the mean

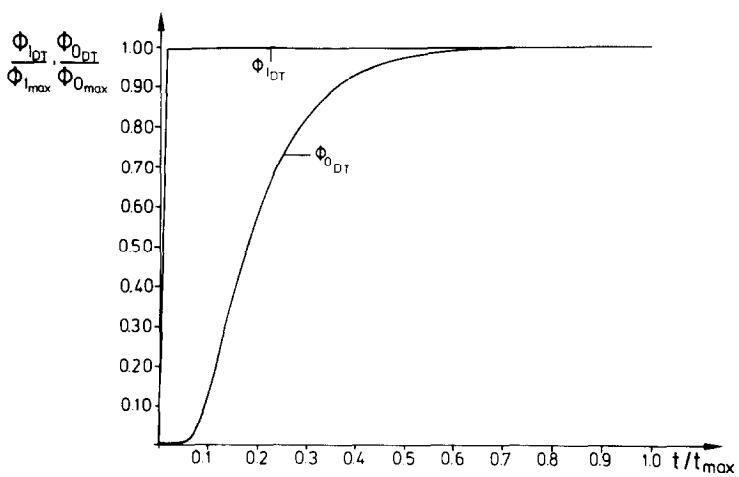

FIG. 12. Time evolution of the nondiagonal recombination fluxes. $\phi_{I_{max}} = 670$ A, $\phi_{O_{max}} = 5.9$ A, $t_{max} = 10^4$ sec.

temperature of which is $T_w = 568°C$. Whereas the density at the inner side saturates almost immediately at $n_T = 5.8 \cdot 10^{17}/cm^3$, the density at the outer side increases slowly to $n_T = 2.3 \cdot 10^{16}/cm^3$. This increase partly causes the recombination processes at the downstream side.

The density profiles of the trapped particle species (Fig. 11) are saturated at the upstream side and nonsaturated at the downstream side. The density of the empty traps reveals the opposite behaviour. The concentration of the empty traps before irradiation is $n_{e_0} = 2.13\ 10^9/cm^3$ and the mean wall temperature is $T_w = 242°C$.

The nondiagonal recombination flux at the upstream side $\phi_{\cdot}$ saturates almost

$\phi_{0_{DT}}$ evolves slowly (Fig. 12) and saturates when the hydrogen buildup is finished.

6. Concluding Remarks

The code provides the possibility to analyze the neutral gas effects inside the first wall and in the plasma. Within the scope of the model assumptions consistency is achieved in the description of the hydrogen buildup in the first wall, the recycling, and the neutral gas and the plasma transport processes. The numerical consistency checks in the first wall and in the neutral gas and the plasma modules show that the computational errors are small. However, uncertainties arise from the nonuniformity of the neutrals' flux densities impinging at the first wall, the unknown backscattering coefficient of the Franck–Condon neutrals and the neglect of adsorption and desorption processes, which might be important at low wall temperatures. Furthermore, the influence of the impurities originating from the eventually coated limiter or first wall might change the plasma behaviour and the correlated recycling processes considerably.

Acknowledgments

The authors thank H. Kever for helpful discussions, Mrs. Boerner for her assistance, Mrs. Bremer for deciphering and typing the manuscript and Mrs. Biermann for the drawings. They are gratefully indebted to H. C. Howe, D. E. Post *et al.*, whose codes PROCTR and AURORA have been the basis for the development of the "first wall module" and the "neutral gas module" used here.

References

1. F. Waelbroeck, P. Wienhold, and J. Winter, *J. Nuclear Mater.* **111/112** (1982), 185.
2. S. J. Fielding, G. M. McCracken, and P. E. Stott, *J. Nuclear Mater.* **76/77** (1978), 273.
3. P. Wienhold, F. Waelbroeck, and J. Winter, *J. Nuclear Mater.* **111/112** (1982), 240.
4. P. Wienhold, I. Ali-Khan, K. J. Dietz, M. Profant, and F. Waelbroeck, *J. Nuclear Mater.* **85/86** (1979), 1001.

5. H. C. HOWE, *J. Nuclear Mater.* **93/94** (1980), 17.
6. C. GILLET, J. HACKMANN, AND J. UHLENBUSCH, *Comput. Phys. Comm.* **24** (1981), 301.
7. K. WILSON AND M. BASKES, *J. Nuclear Mater.* **76/77** (1978), 291.
8. T. J. DOLAN, *J. Nuclear Mater.* **92** (1980), 112.
9. P. WIENHOLD, F. WAELBROECK, J. WINTER, AND I. ALI-KHAN, Report Jül 1964 (1980).
10. O. S. OEN AND M. T. ROBINSON, *Inst. Phys. Conf. Ser.* **28** (1976), 329.
11. M. H. HUGHES AND D. E. POST, *J. Comput. Phys.* **28** (1978), 43.
12. M. BROUDEUR, Thesis, 1978, CEA-R-4701.
13. M. BRAUN, B. EMMOTH, F. WAELBROECK, AND P. WIELHOLD, *J. Nuclear Mater.* **93/94** (1980), 861.
14. F. WAELBROECK, J. WINTER, AND P. WIENHOLD, *J. Nuclear Mater.* **103/104** (1981), 471.
15. "Dubbels Taschenbuch für den Maschinenbau," 11th ed., Springer-Verlag, Berlin/New York, 1958.
16. H. C. HOWE, *J. Nuclear Mater.* **111/112** (1982), 424.
17. D. REITER AND A. NICOLAI, *J. Nuclear Mater.* **111/112** (1982), 434.
18. A. C. RIVIERE, *Nuclear Fusion* **11** (1971), 363.
19. R. D. BENGTSON, "Proceedings, Conference Concerning Diagnostics for Fusion Experiments, Vienna, September 4–16, 1978," Pergamon, New York, 1979.
20. M. H. KALOS, F. R. NAKACHE, AND J. CELNIK, "Computing Methods in Reactor Physics," Chapter 5, Gordon & Breach, New York, 1968.
21. R. BEHRISCH, Summer School of Tokomak Reactors for Breakeven, Erice, 1976.
22. T. TABATA, R. ITO, Y. ITIKAWA, N. ITOH, AND K. MORITA, Report IPPJ-AM-18, 1981.
23. W. ECKSTEIN AND H. VERBEEK, Report IPP 9/32, 1979.
24. O. S. OEN AND M. T. ROBINSON, *J. Nuclear Mater.* **76/77** (1978), 370.
25. D. HEIFETZ, D. POST, M. PETRAVIC, J. WEISHEIT, AND G. BATEMAN, *J. Comput. Phys.* **46** (1982), 309.
26. G. RITTER, "Untersuchungen zum Neutralteilchenverhalten in einem Tokamak Plasma," Dissertation, Univ. Düsseldorf, 1982. J. HACKMANN, C. GILLET, G. REINHOLD, G. RITTER, AND J. UHLENBUSCH, *J. Nuclear Mater.* **111/112** (1982), 221.
27. A. RÉNYI, "Wahrscheinlichkeitsrechnung," Deut. Verlag Wissenschaften, Berlin, 1979.
28. Y. SEKI *et al.*, *Nuclear Fusion* **20** (1980), 10.
29. D. HEIFETZ, D. POST, M. ULRICKSON, AND J. SCHMIDT, *J. Nuclear Mater.* **111/112** (1982), 298.
30. J. T. HOGAN, Multifluid Tokamak transport models, *in* "Methods in Computational Physics," Vol. 16, Academic Press, New York, 1976.
31. D. F. DÜCHS, P. E. POST, AND P. H. RUTHERFORD, *Nuclear Fusion* **17** (1977), 565.
32. R. H. FOWLER AND J. A. ROME, Report ORNL/TM 6845, 1979.
33. J. T. HOGAN, *Nuclear Fusion* **21** (1981), 365.
34. F. L. HINTON AND R. D. HAZELTINE, *Rev. Modern Phys.* **48** (1976), 239.
35. W. ENGELHARDT, K. BEHRINGER, AND G. FUSSMANN, Verhandlungen der Deutschen Physikalischen Gesellschaft, Frühjahrstagung Hamburg vom 23.–27.3.1981, Vortrag P3.
36. The INTOR group, *Nuclear Fusion* **22** (1982), 135.
37. M. F. A. HARRISON *et al.*, Report CLM-R 211.
38. K. LACKNER *et al.*, NET Report EUR XII-324/5.